Insight into the Mechanism of Graphene Oxide Degradation via the Photo-Fenton Reaction

Hao Bai,[†] Wentao Jiang,[†] Gregg P. Kotchey,[†] Wissam A. Saidi,[‡] Benjamin J. Bythell,[§] Jacqueline M. Jarvis,[§] Alan G. Marshall,[§,∥] Renã A. S. Robinson,[†] and Alexander Star*,[†]

[†]Department of Chemistry and [‡]Department of Chemical and Petroleum Engineering, University of Pittsburgh, Pittsburgh, Pennsylvania 15260, United States

[§]National High Magnetic Field Laboratory, Florida State University, 1800 E. Paul Dirac Drive, Tallahassee, Florida 32310, United States

[∥]Department of Chemistry and Biochemistry, Florida State University, 95 Chieftain Way, Tallahassee, Florida 32306, United States

S *Supporting Information*

ABSTRACT: Graphene represents an attractive two-dimensional carbon-based nanomaterial that holds great promise for applications such as electronics, batteries, sensors, and composite materials. Recent work has demonstrated that carbon-based nanomaterials are degradable/biodegradable, but little work has been expended to identify products formed during the degradation process. As these products may have toxicological implications that could leach into the environment or the human body, insight into the mechanism and structural elucidation remain important as carbon-based nanomaterials become commercialized. We provide insight into a potential mechanism of graphene oxide degradation via the photo-Fenton reaction. We have determined that after 1 day of treatment intermediate oxidation products (with MW 150−1000 Da) were generated. Upon longer reaction times (i.e., days 2 and 3), these products were no longer present in high abundance, and the system was dominated by graphene quantum dots (GQDs). On the basis of FTIR, MS, and NMR data, potential structures for these oxidation products, which consist of oxidized polycyclic aromatic hydrocarbons, are proposed.
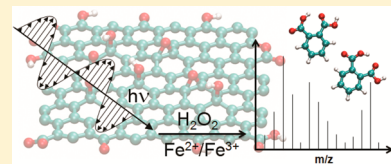
INTRODUCTION

Graphene, a single layer of sp^2-hybridized carbon atoms bonded together in a hexagonal lattice, has garnered widespread excitement within the scientific community as a result of its unique physical properties.[1−3] These attributes have catalyzed ground-breaking research, where graphene is employed for applications, including electronics, batteries, sensors, and composite materials.[1,2,4−6]

A bulk, solution-based methodology for producing graphene-based derivatives entails exfoliating graphite via chemical oxidation and subsequently employing sonomechanical treatment to yield graphene oxide (GO).[7,8] Although the structure of GO has been debated in the literature,[7] one model holds that GO consists of sp^3-hybridized carbon domains on the basal plane to which tertiary alcohols and epoxy functional groups are attached; carboxylic acid, keto, and 5- and 6-membered lactol groups decorate the edge.[9−12] In addition, there exist nonoxidized sp^2 segments that are either aromatic or conjugated.[11] GO and its reduced form, reduced GO (rGO), represent carbon-based nanomaterials that have been utilized for diverse applications, including field-effect transistor devices, sensors, clean energy devices (e.g., rechargeable lithium ion batteries (RLBs), and electrochemical double layer capacitors (EDLCs)).[2]

Upon treatment (e.g., acid oxidation,[13,14] hydrothermal,[15,16] solvothermal,[17,18] microwave,[19] or the photo-Fenton reaction[20]), GO is susceptible to further oxidation wherein the epoxy groups are converted into more energetically favorable carbonyl moieties. This process ruptures the underlying C−C bonds, thereby resulting in the formation of small carbonaceous particles called graphene quantum dots (GQDs) that contain nanometer-size aromatic sp^2 domains surrounded by oxygen moieties along the edges.[21] Endowed with photoluminescence and low cytotoxicity, GQDs hold great promise for biomedical applications such as bioimaging and drug delivery.[21]

A growing area of research entails the biodegradation of carbon-based nanomaterials to alleviate toxicity of this nanomaterial, facilitate drug delivery, and promote environmental remediation applications.[22−26] In particular, peroxidases such as horseradish peroxidase (HRP), myeloperoxidase, and eosinophil peroxidase have been demonstrated to degrade both carbon nanotubes and graphene oxide. Although the degradation products of myeloperoxidase were shown not to induce toxicity,[23] recently, the oxidation products (e.g., MW < 3000 Da) of HRP-catalyzed degradation of SWCNTs have been identified to induce DNA damage;[27] in that study, however, no structures were identified. Therefore, structural elucidation of the degradation products of carbon nanomaterials represents a relevant and fundamentally important step with implications for diverse fields. In our work, we selected GO and the photo-

Fenton reaction to oxidize this carbon nanomaterial as a result of the relative ease to work with GO in solution and because the photo-Fenton reaction is a mass spectrometry (MS) friendly oxidation method.

Since the 1894 discovery by Henry Fenton that tartaric acid undergoes oxidation in the presence of hydrogen peroxide and trace amounts of ferrous salts (i.e., the Fenton reagents),[28] this reaction has been systematically studied,[28−30] developed,[30−36] and expanded to numerous applications[30,31] including the remediation of polycyclic aromatic hydrocarbons (PAHs) in wastewater.[22,23] It is widely accepted that the oxidative species of the Fenton mechanism consist of radicals including the highly reactive hydroxyl (·OH) radical,[37] and the introduction of ultraviolet (UV) irradiation to the system accelerates the production of this radical species.[38]

Recently, the Fenton reaction has been employed to degrade carbon-based nanomaterials such as carbon nanotubes (CNTs)[39] and graphene oxide (GO).[20] In the latter work, the authors demonstrated that the photo-Fenton reaction was both an effective and efficient method for oxidizing graphene oxide into GQDs. In our work, a similar reaction is performed on commercially fabricated GO. By use of several analytical techniques, specifically mass spectrometry (MS), attenuated total reflectance-Fourier transform infrared (ATR-FTIR) spectroscopy, and nuclear magnetic resonance (NMR) spectroscopy, we focus on the identification of a few intermediate oxidation products (i.e., small molecules with molecular weights <1000 Da) and GQDs that arise from the photo-Fenton reaction over the course of several days. In addition, employing atomic force microscopy (AFM), we monitor the morphological transformation of graphene oxide flakes. Finally, density functional theory (DFT) calculations provide insight into the mechanism of degradation/GQD formation. From these techniques, we demonstrate that the early stage of photo-Fenton-catalyzed degradation of GO yields small molecules for which we propose plausible structures based on their tandem MS and NMR spectra. Moreover, after longer reaction time, we observe the formation of holes on the basal plane of the GO sheets, and the GO flakes begin to break apart into individual islands that are known as GQDs.

EXPERIMENTAL METHODS

Reagents and Materials. All of the reagents were used as received without further purification. Graphene Oxide (GO) (5 mg mL^{-1}) was purchased from Graphene Laboratories, Inc. (Calverton, NY) in an aqueous solution. FeCl$_3$ (hexahydrate), 30% H$_2$O$_2$, and concentrated HCl were purchased from Sigma-Aldrich Corp. (St. Louis, MO). Solvents, including H$_2$O, ACN, and MeOH were acquired from ThermoFisher Scientific (Pittsburgh, PA) at HPLC grade or higher.

The Photo-Fenton Reaction. The photo-Fenton reaction was carried out under vigorous stirring in a 50 mL quartz tube, which was held ∼6 cm from a UV lamp (Blak-Ray B100AP, 100-W long wave UV, which produces fluorescence with a ballasted bulb). In a typical experiment, 500 μL of 5 mg mL^{-1} GO aqueous solution, 4.5 μL of 30% H$_2$O$_2$, 100 μL of 1 mM FeCl$_3$, and 24.6 mL nanopure H$_2$O were mixed in the quartz tube. The pH of the mixture was adjusted to pH 4 with HCl. The tube was sealed and 4.5 μL of 30% H$_2$O$_2$ was added on a daily basis to observe a complete degradation of GO during 3 days. After the reaction, the sample was passed through a 0.22 μm TefSep PTFE membrane filter (GE Infrastructure Water & Process Technologies, Trevose, PA). Partially oxidized GO was

collected, and its mass was measured on the filter after overnight drying in an oven (ThermoFisher Scientific, Pittsburgh, PA). The filtrate was dried via lyophilization (Labconco Freezone 6 Lyophilizer, Kansas City, MO).

AFM. A Veeco Dimension 3100 (Plainview, NY) atomic force microscope was utilized in tapping mode for thickness, phase, and sectional analysis. Sample preparation was performed on a freshly washed Si wafer treated with piranha solution (7:3 concentrated H$_2$SO$_4$/30% H$_2$O$_2$, 70 °C). Approximately 10 μL of the sample (aq) was spin-coated at 1400 rpm to obtain an evenly distributed sample on the wafer surface.

Raman Spectroscopy. Samples were prepared by spin-coating approximately 10 μL of graphene oxide solution at day 0, day 1, and day 3 at 1400 rpm on freshly cleaned silica wafers (treated with piranha solution). All spectra were obtained with a Renishaw inVia Raman microscope at an excitation wavelength of 633 nm. Ten scans from 1000 to 3000 cm^{-1} were acquired and averaged to determine the D and G band ratio.

Nuclear Magnetic Resonance (NMR). The lyophilized day 1 degradation products were resuspended in D$_2$O to prepare a solution with a final concentration of ∼5 mg mL^{-1}. NMR spectra, including ^{1}H, ^{13}C, correlated spectroscopy (COSY), heteronuclear multiple-bond correlation (HMBC), and heteronuclear multiple quantum coherence (HMQC) spectra were acquired by use of a Bruker Avance III 400 MHz NMR spectrometer and a Bruker Avance III 500 MHz NMR spectrometer (Billerica, MA).

LDI Mass Spectrometry. A Voyager-DE PRO MALDI TOF mass spectrometer (AB Sciex, Framingham, MA) was utilized for LDI data. Filtered/lyophilized day 0, 1, and 3 samples were resuspended in nanopure water at a concentration of 0.2 mg mL^{-1} and tested without any matrix. To this end, 10 μL of sample solution was dropped onto a MALDI plate and dried under ambient conditions. For data acquisition, the instrument settings were positive reflector mode; 25 000 V accelerating voltage, grid voltage equals 75% accelerating voltage, 1.12 mirror to accelerating voltage ratio, 200 ns extraction delay, and 2500 laser intensity with N$_2$ laser source.

ESI Orbitrap Mass Spectrometry. An LTQ Orbitrap-Velos mass spectrometer (Thermo Fisher Scientific) was employed for mass spectra acquisition. Filtered/lyophilized day 0, 1, and 3 samples (1 mg mL^{-1}) were resuspended in 50:50 (v/v) H$_2$O/MeOH or 50:50 (v/v) H$_2$O/ACN with 0.1% formic acid (FA) and directly infused into the ESI source at a flow rate of 3 μL min^{-1}. Data were collected in positive ion mode. The voltage of the ESI tip was held at 4.5 kV, sheath gas was employed, and the entrance capillary was maintained at 275 °C. Precursor ion mass spectra were obtained in the Orbitrap at 60 000 nominal resolving power at m/z 400, and selected ions were fragmented in the dual-pressure LTQ with collision-induced dissociation at normalized collision energy 35% and injection time 25 ms. MS/MS data were recorded in the Orbitrap at 60 000 nominal resolving power at m/z 400 unless otherwise noted.

ESI-FTICR. These experiments were performed with a custom-built 9.4 T ESI FT-ICR mass spectrometer recently described in detail.[40,41] Samples were infused into a tapered 50 μm i.d. fused silica micro-ESI needle[42,43] at a rate of 300−500 nL min^{-1} at a concentration of ∼10 μM. ESI conditions were the following: needle voltage 2 kV and heated capillary current 4.0 A. One volt was applied to the end-cap and compensation

electrodes of the ICR cell.[41] The analyte ions were isolated by stored waveform inverse Fourier transform (SWIFT).[44,45] Mass-selective ion ejection and irradiation were implemented with a Synrad (Mukilteo, WA) CW CO_2 laser ($\lambda = 10.6$ μm).[46,47] Following irradiation, the remaining precursor and fragment ions were excited to higher radius and then detected. Typical (uncorrected) base pressure for the instrument was $\leq 2 \times 10^{-10}$ Torr, measured by a Bayard-Alpert ionization gauge.

Instrument control, data acquisition, and data analysis were carried out with a modular ICR data station.[48] Each time-domain ICR signal was Hanning apodized,[49] zero-filled once,[49] and Fourier transformed to generate a magnitude-mode spectrum that is converted to mass-to-charge ratio by a two term calibration equation.[50]

Spectrofluorometry. Samples of graphene oxide solution at day 0, day 1, and day 3 of the photo-Fenton reaction were diluted 5-fold, and their fluorescence spectra were measured with a Fluoromax 3 spectrometer (Horiba Scientific, Edison, NJ, USA). Measurements were acquired every 0.5 nm from 350 to 625 nm at an excitation wavelength of 325 nm. Water was employed as the background and subtracted from the resulting spectra for day 0, day 1, and day 3.

ATR-FTIR Spectroscopy. To obtain IR spectra of both dried GO and lyophilized samples of products after day 1 of degradation, a Nicolet iS5 (Thermo Fisher Scientific, Pittsburgh, PA) FTIR spectrometer outfitted with a diamond ATR accessory was employed. Sixty-four scans were implemented per sample, and the spectra were treated with ATR and atmosphere correction.

Density Functional Theory Calculations. The quantum-mechanical DFT calculations were carried out by use of Gaussian 09,[51] where the exchange-correlation functional was approximated based on B3LYP.[52−55] The orbitals are expanded by use of a 6-311+G(d,p) atomic basis set.[56,57] We related all atomic coordinates with tight convergence thresholds. The GQD was modeled with an armchair and zigzag edges.

■ RESULTS

Trace amounts of H_2O_2 and Fe^{2+}/Fe^{3+} can be removed via lyophilization. Therefore, the photo-Fenton reaction represents an MS-friendly process for elucidating the intermediate oxidation products of GO. Adjusting the power of the UV lamp enables effective control over the degradation reaction rate (Figure 1A). AFM was employed to analyze the size and thickness of the flakes extracted from the bulk dispersion of GO. The mean size of this carbon nanomaterial has a broad distribution of 589 ± 700 nm, and the flake thickness is 0.972 nm, which represents a single-layer of GO (Supporting Information Figure S1).[58,59] After 1 day of incubation under the photo-Fenton conditions, the GO flakes in the dispersion are more narrowly distributed in size, undergo ∼40% reduction to 358 ± 186 nm, and demonstrate a thickness increase of ∼15% versus day 0, which may be attributed to further oxidation. After the photo-Fenton reaction proceeds for 3 days, small particles with a mean diameter of 36 ± 10 nm and thickness ranging from 2 to 5 nm are present. These data indicate that graphene quantum dots (GQDs) are successfully formed from the oxidation of GO, and in the bulk dispersion the GQDs exist as multiple layers due to van der Waals interactions.

To analyze the morphological changes of the same individual GO flakes, a dispersion consisting of GO was spin-coated onto a Si wafer, and the GO/Si substrate was subsequently subjected
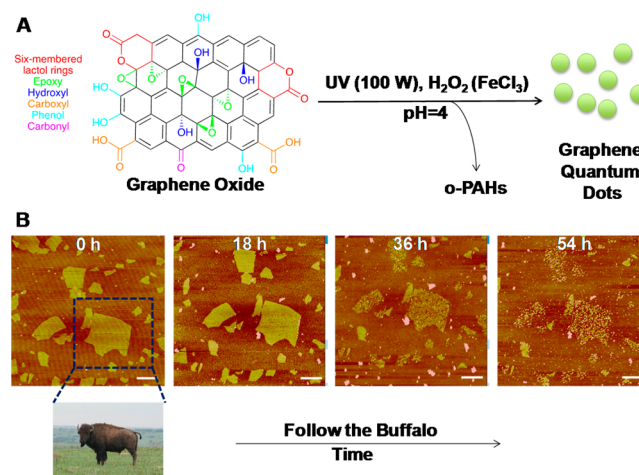

Figure 1. (A) Schematic diagram demonstrating the degradation of graphene oxide (GO) via the photo-Fenton reaction, which results in the formation of oxidized polycyclic aromatic hydrocarbon (o-PAH) intermediates and graphene quantum dots (GQDs) products with time. (B) AFM images of as-received GO after reaction with the Fenton reagent under UV irradiation for 0, 18, 36, and 54 h. All images were obtained in tapping mode, and the scale bars are 500 nm.

to the photo-Fenton reaction at 18 h intervals (Figure 1B). AFM section analysis demonstrates that after 18 h, the thickness of the GO flakes increases by ∼80% (i.e., from around 1.41 ± 0.36 to 2.49 ± 0.14 nm, Supporting Information Figure S2A,B). To ascertain the origin of the thickness increase, control experiments were conducted (Supporting Information Figure S3). After 18 h under UV exposure without the Fenton reagents, the thickness of the GO remains roughly the same (i.e., a 4% increase in thickness over 36 h); a similar trend was likewise observed when the Fenton reagents were present in solution in the absence of UV exposure (i.e., a 5% decrease in thickness over 36 h). Therefore, given the absence of a significant change in thickness for the controls, one plausible explanation for the observed change in thickness after 18 h of UV-driven oxidation could be the formation of reaction products that adsorb to the GO sheet thereby forming an additional layer. After an additional 18 h of the photo-Fenton reaction (i.e., a total of 36 h), holes were observed on the basal plane of the GO sheets, and the overall thickness of the flakes decreased by 56 and 22% relative to 18 and 0 h (Supporting Information Figure S2D). Finally, after 54 h of the photo-Fenton reaction, most of the GO flakes were oxidized into GQDs with a thickness of 2.04 nm (Supporting Information Figure S2E).

Raman spectroscopy was employed to further analyze the oxidation of GO catalyzed by the photo-Fenton reaction. For the sample that consists of GO in solution, the ratio of the defect induced D-band relative to the G-band, which results from the stretching of C−C bonds in a graphitic lattice (i.e., the D/G ratio)[60] decreases by 19% from 2.19 at day 0 to 1.84 by day 1, and no bands that are characteristic of GO are observed at day 3 (Supporting Information Figure S4A). On the other hand, for the sample that was spin-coated onto the Si substrate, the Raman signature for GO, which initially had a D/G ratio of 2.28, is not observed after 18 h of the photo-Fenton reaction (Supporting Information Figure S4B).

As seen in Figure 2A, the GO solution, which is initially dark brown in color, became lighter and virtually colorless with time, this providing empirical evidence of GO oxidation catalyzed by
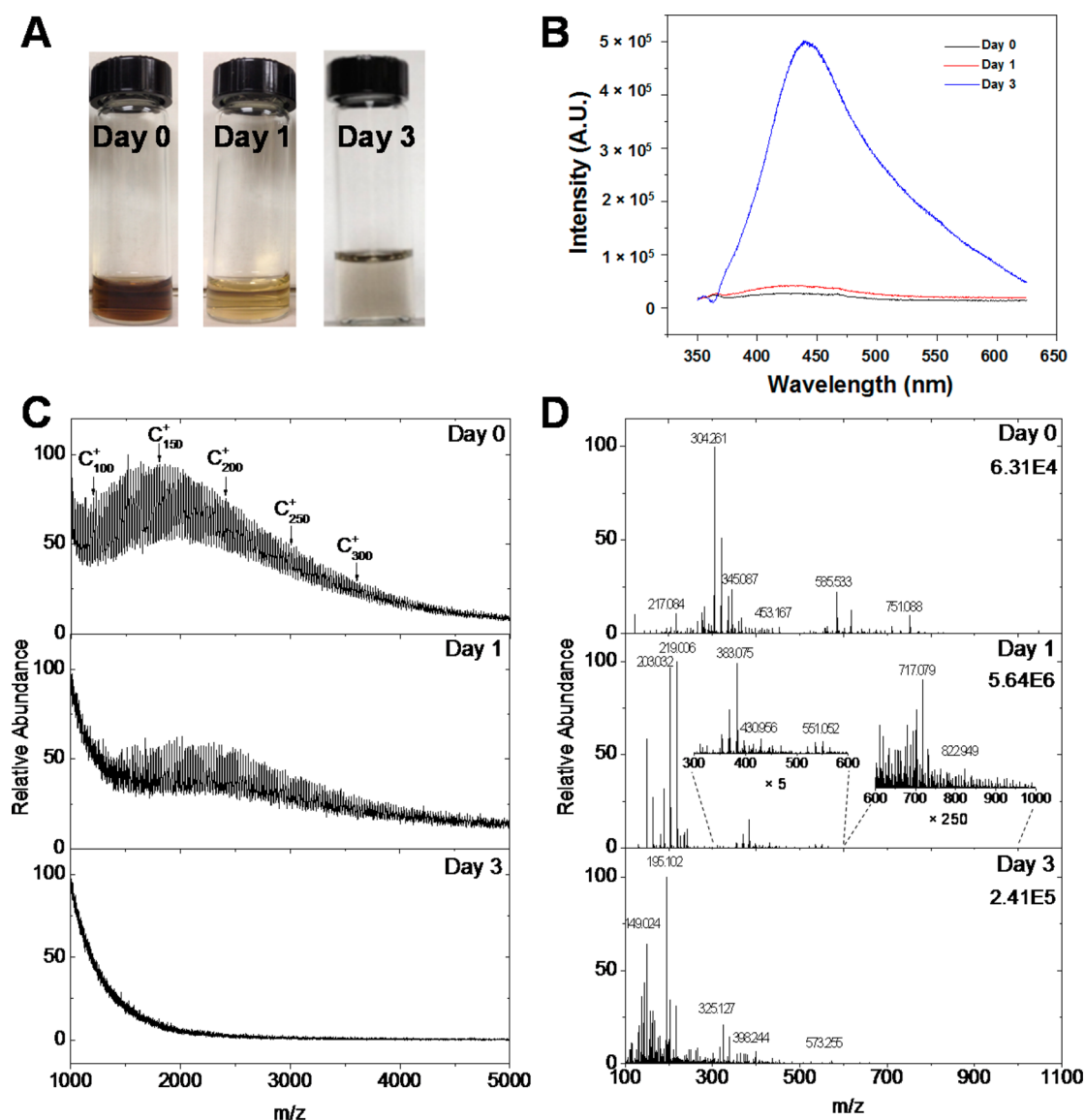
Figure 2. (A) Photograph depicting vials of graphene oxide solution after 0, 1, and 3 days of the photo-Fenton reaction. (B) Fluorescence spectra of the solutions contained in (A). (C) LDI-TOF MS and (D) Orbitrap ESI-MS spectra for sample after 0, 1, and 3 days of the photo-Fenton reaction.

the photo-Fenton reaction. The fluorescence of the starting material (i.e., GO) and products derived from the photo-Fenton reaction after 1 and 3 days was examined (Figure 2B). Upon excitation at 325 nm, GO demonstrates a broad peak that is centered on 430 nm. By day 1, the fluorescent intensity increased 154% versus day 0, and its spectrum is both broad and centered on 430 nm. Finally, the fluorescence intensity on day 3 increases 1814 and 1175% versus day 0 and 1, and its sharp peak is centered at ~440 nm. This increase in fluorescence provides evidence that GO is broken down into conjugated products (e.g., oxidized PAHs and/or GQDs).

MS was implemented to elucidate the products of oxidation. Figure 2C depicts the laser desorption ionization (LDI) time-of-flight (TOF) mass spectra corresponding to products obtained at days 0, 1, and 3 after the start of the photo-Fenton reaction. The LDI TOF MS data reveal the presence of carbon clusters ranging from 1000 to 5000 Da ($\sim C_{100}$ to C_{400}) in the day 0 and day 1 sample (Figure 2C); these large clusters are not observed in the day 3 sample (Figure 2C). Carbon cluster peaks are spaced by 24 Da across the mass spectra and

correspond to the mass of two carbon atoms. It should be noted that because these peaks correspond to carbon clusters smaller in size than the flakes detected by AFM, these clusters may represent fragments generated via laser ablation of larger flakes of GO. By day 3, large GO flakes are broken down into smaller quantum dots (as evidenced by AFM); therefore, the carbon cluster ions do not appear in the MS spectrum.

Figure 2D displays the electrospray ionization (ESI)-Orbitrap MS spectra of degradation products on days 0, 1, and 3. As observed from the spectra, larger magnitude signal and features are present on day 1 in comparison to days 0 and 3. In particular, numerous peaks are detected from m/z 300–1000 on day 1.

The ESI-Orbitrap MS findings for day 1 degradation products were compared to MS data obtained by 9.4 T ESI Fourier transform ion cyclotron resonance (FT-ICR) MS. Supporting Information Figure S5 compares the precursor ion mass spectra obtained. There is considerable overlap between ions observed from both analyses despite variations in the

10522

dx.doi.org/10.1021/jp503413s | J. Phys. Chem. C 2014, 118, 10519–10529
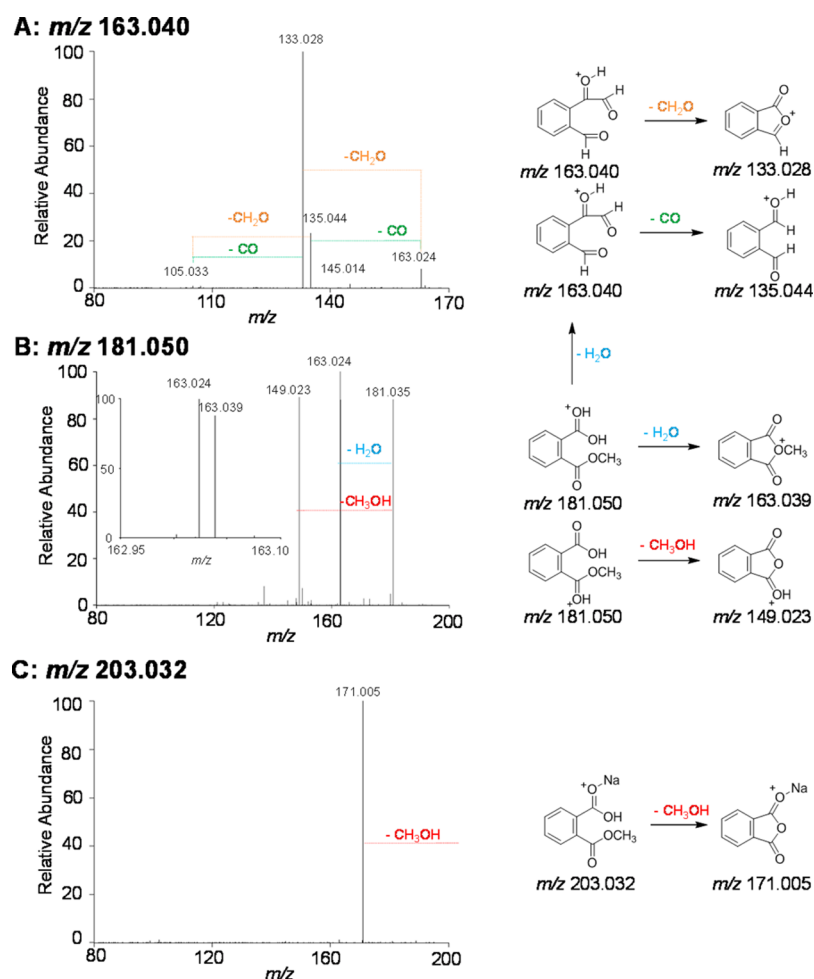
Figure 3. Orbitrap MS/MS results for precursor ions of m/z (A) 163.040, (B) 181.050, and (C) 203.032. Structures for (A–C) and proposed fragmentation pathways are shown on the right.

magnitude of signal, which may be partially attributable to inherent differences in the source conditions.

High mass measurement accuracy obtainable with both instruments was used to make assignments of elemental composition. Because of the complexity of the data sets, however, only selected species were isolated and exposed to gas-phase fragmentation in order to better deduce chemical composition and possible structures.

For example, peaks at m/z 149.024, 163.040, 189.017, and 203.032, which have the greatest magnitude in the parent scans of the Orbitrap MS data, demonstrate the fragmentation patterns observed in Figure 3 and Supporting Information Figure S6. In the low m/z region of the parent spectrum (Orbitrap MS), a series of peaks related to phthalic acid is observed as follows: the protonated phthalic acid peak (m/z 167.034, $[C_8H_6O_4 + H]^+$, −0.56 ppm), a potassiated acid peak (m/z 204.990, $[C_8H_6O_4 + K]^+$, −0.81 ppm), protonated phthalic anhydride (m/z 149.024, $[C_8H_4O_3 + H]^+$, −0.06 ppm), and the fragment species of protonated phthalic anhydride with the loss of a neutral CO molecule (m/z 121.029, $[C_7H_4O_2 + H]^+$, −1.61 ppm). To confirm the assignment of these peaks, a standard solution of phthalic acid was also analyzed by ESI-Orbitrap MS and the mass spectrum has similar distributions in the precursor and MS/MS data from the day 1 sample (Supporting Information Figure S6). Building on the phthalic acid peaks, the ion at m/z 181.050 (Figure 3B)

has been assigned to monomethyl phthalate. The monomethyl phthalate ion was observed in the parent spectrum both as a sodiated acid precursor (m/z 203.032, $[C_9H_8O_4 + Na]^+$, 1.83 ppm) and as the protonated anhydrous monomethyl phthalate species (m/z 163.040, $[C_9H_6O_3 + H]^+$, −0.12 ppm). MS/MS of m/z 181.050 produces fragment peaks corresponding to the loss of methanol and water. The anhydride at m/z 163.040 undergoes two fragmentation pathways (Figure 3A) corresponding to neutral losses of CO or CH_2O. Further support for these assignments is provided by the MS/MS results for the sodiated adduct of monomethyl phthalate (Figure 3C). A single fragment peak corresponding to the loss of the neutral methanol is observed. The significant energetic barrier to loss of neutral NaOH (305 kJ mol^{-1}) from the protonated, cyclic anhydride species prevents the alternate fragmentation pathway. We note that a fragment peak corresponding to the loss of water would be expected if the methyl group were a substituent on the benzene ring. Some B3LYP/6-31+g(d,p) calculations relevant to the above discussion are shown in Supporting Information Scheme S1.

On the basis of the errors associated with the peaks in the precursor and fragment mass spectra and the associated calculated degrees of unsaturation, aromatic rings and the presence of C=O bonds are necessary. Structural information is limited to adjacent aromatic rings or anhydride structures. The ion observed at m/z 389.01855 in both data sets was

selected for FT-ICR MS/MS (Figure 4). This species was assigned an elemental composition ($[C_{16}H_{13}O_9Ca]^+$, −0.3 ppm
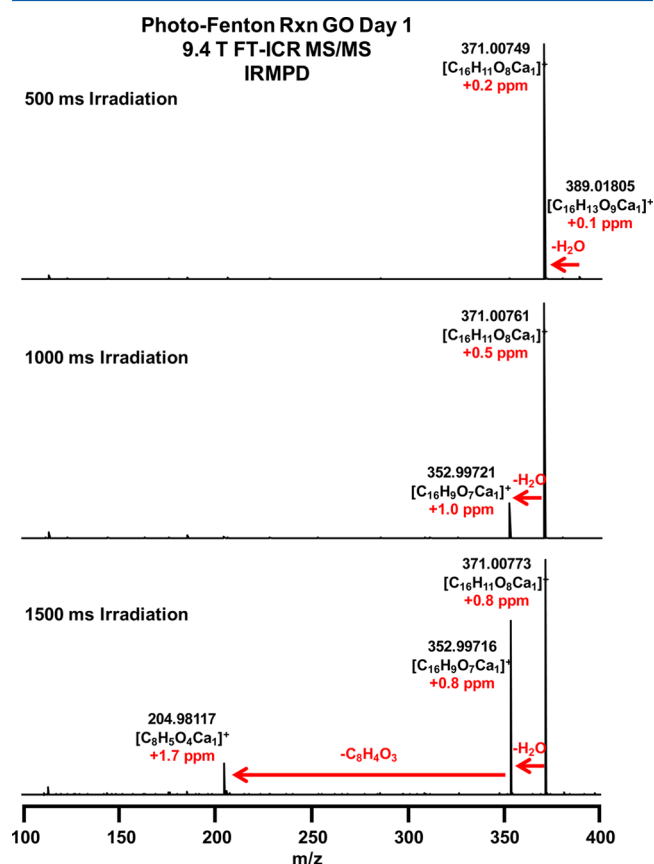
Figure 4. FT-ICR mass spectra following IRMPD fragmentation of precursor ion (m/z 389.01805, $[C_{16}H_{13}O_9Ca]^+$) after irradiation for 500, 1000, and 1500 ms.

error) based upon isotopic verification (Figure 4). After short irradiation periods (Figure 4, top and middle), sequential neutral losses of m/z 18 yielded a fragment ion at m/z 352.99721 ($[C_{16}H_9O_7Ca]^+$). After longer irradiation (Figure 4, bottom), an additional neutral loss of m/z 148 ($C_8H_4O_3$) was observed (also by Orbitrap MS/MS).

Similar FT-ICR MS/MS behavior is seen in Supporting Information Figure S7, for precursor ions of m/z 703 ($[C_{32}H_{23}O_{16}Ca]^+$, this time with successive neutral losses of $C_8H_6O_4$, which is also observed in Orbitrap MS/MS (data not shown). It is worth noting that elemental compositions could be assigned to other neutral losses, even in cases for which the precursor ion composition could not be assigned. Thus, we have high confidence in the assignments for neutral losses.

The difficulty in assigning elemental compositions is illustrated by Supporting Information Table S1, listing the accurate masses of the 20 most abundant species observed by FT-ICR MS. Even with internal calibration, about half of the peaks could not be assigned by allowing for up to one Na, one K, and two Ca atoms in addition to C, H, and O. It should be noted that in each case we required resolution and identification of at least one heavy heteroatom isotope (e.g., ^{18}O, ^{40}K, ^{43}Ca) with mass spectral peak magnitude greater than 6σ of baseline noise for valid assignment. One could of course allow for more elements; however, the number of possible elemental compositions thereby also increases, so that even

higher mass resolving power is needed. In any case, our intent was not to achieve complete compositional assignment, but rather to identify major components (and fragmentation losses) confidently.

Overall, the ESI-MS data point to the presence of degradation products that are higher in abundance at day 1 than for days 0 and 3. This observation supports the hypothesis that oxygen sites on GO are oxidized immediately after the initiation of the photo-Fenton reaction, and when combined with the degradation of GO flakes, intermediate species (with MW 150−1000) are generated by day 1. After a period of time between day 1 and 3, these intermediates are no longer prominently present, and the system is dominated by GQDs.

Further evidence for the proposed functional groups of the day 1 degradation products was assessed by ^1H NMR, ^{13}C NMR, and three types of 2D NMR, including correlation spectroscopy (COSY), heteronuclear multiple quantum coherence (HMQC) for direct C−H coupling, and heteronuclear multiple bond coherence (HMBC) for 2−4 bond coupling.

The ^1H NMR spectrum in D_2O (Figure 5A) indicates the presence of aromatic protons (i.e., 7.61 and 7.49 ppm), methyl benzoate protons (4.03 ppm) and signals that can be assigned to benzyl protons in the region of 2.5 to 2.8 ppm. Because there exists a possibility of exchange with the deuterium in the solvent, no signals from labile protons, such as −COOH and/ or −OH, were observed. The COSY spectrum (Figure 5B) depicts the proton coupling through a limited number of chemical bonds (usually less than 4). The peaks can be divided into two groups: diagonal peaks sharing the same frequency coordinate as each axis and off-diagonal or cross peaks indicating the couplings between pairs of protons. The latter is what we want to focus on. The blue arrow segment can be assigned to the multiple aromatic protons, and the green arrow indicates the coupling between methyl/benzyl protons. The red arrow denotes coupling between benzyl protons and ortho hydrogens on aromatic rings.

Although not enough information is available about the functional groups obtained from proton NMR subject to the proton exchange mentioned above, the ^{13}C spectrum (Supporting Information Figure S8A) indicates characteristic peaks for aromatic carbons (128−132 ppm) and carboxylic acid groups (172 ppm). Therefore, the ^{13}C spectrum supports the presence of oxygen-containing functional groups. In HMQC (Supporting Information Figure S8B), which represents the direct C−H coupling, the relationship between adjacent hydrogen and carbon nuclei is reflected. Besides aromatic protons, various oxygen-containing functional groups, as expected, can appear in the oxidation products. Although the degree of unsaturation is high, as noted from the MS data, there are still methyl protons. In addition to the direct coupling, HMBC (Supporting Information Figure S9), indicating coherent 2−4 bond coupling, provided strong evidence of carboxylic acid functionality, aiding in structural elucidation.

Attenuated total reflectance-Fourier transform infrared (ATR-FTIR) spectroscopy was employed to elucidate further insight into the functional groups in the degradation products. The spectrum of GO was compared to the degradation products formed after 1 day of the photo-Fenton reaction (Supporting Information Figure S10). For both samples, the peaks overlapped and were identified at 3465 (C−OH vibrations), 2997, 2914, 1735 (C=O, carboxyl), 1428, 1365 (epoxide, C−O−C), and 1215 cm^{-1} (C=O).[61] Therefore, the ATR-FTIR data indicate that the products at day 1 contain
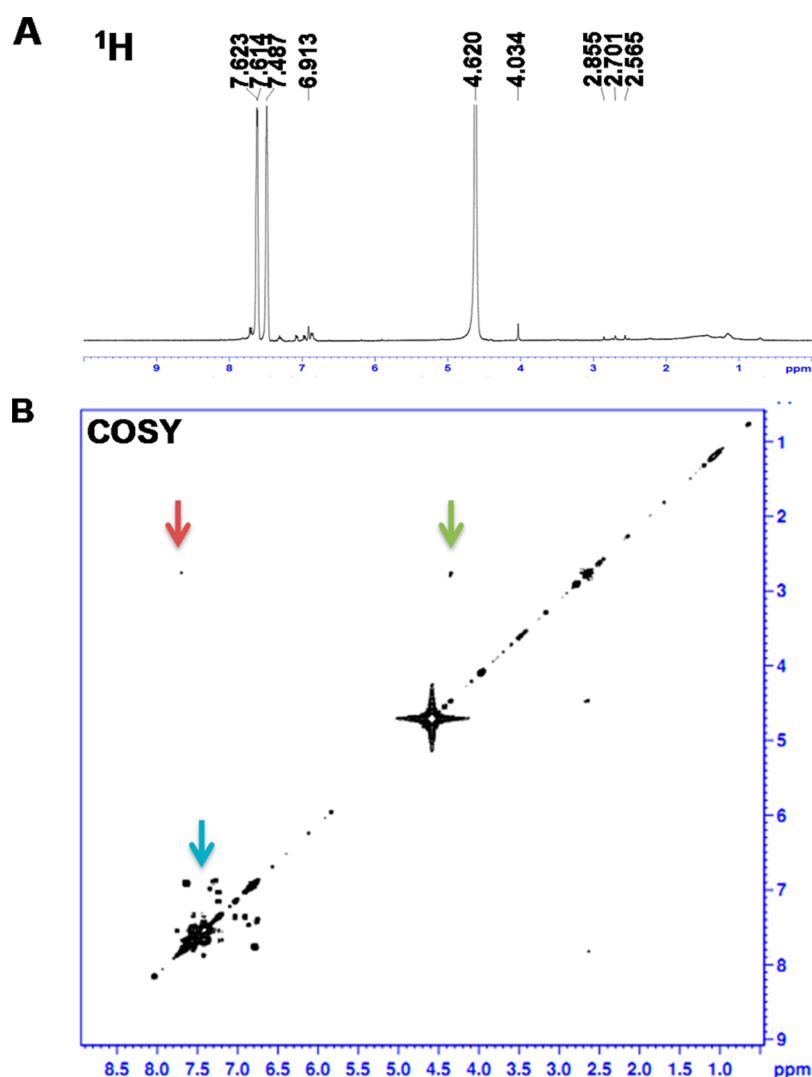
Figure 5. (A) 1D ^{1}H NMR spectrum (D$_2$O) and (B) 2D correlation (COSY) NMR spectrum of the day 1 oxidation products produced via the photo-Fenton reaction with GO.

similar functional groups as GO, including carboxyl functional groups.

DISCUSSION

Insight into the mechanism of photo-Fenton-catalyzed oxidation of graphene oxide can be inferred from previous experiments, in which the Fenton reaction was employed to generate hydroxyl radicals, which subsequently reacted with carbon nanotubes (CNTs).[62] In that work, hydroxyl radicals oxidized CNTs by two mechanisms. First, in an approximately single-phase reaction, the hydroxyl radicals imparted carboxylic acids at the defect sites, and these oxygen moieties were subsequently further oxidized to CO$_2$ and H$_2$O.[62] For the second pathway, hydroxyl radicals undergo electrophilic addition on unsaturated bonds yielding hydroxylated CNTs.[62] Next, the hydroxylated CNTs undergo further oxidation whereby the hydroxyl groups were converted into quinones.[62] Finally, the strong oxidizing environment facilitates the conversion of the quinone groups to carboxylic acids, which can be further broken down into CO$_2$ and H$_2$O.[62] In this work, our starting material, GO, already consists of sp^3-hybridized carbon domains on the basal plane to which tertiary alcohols and epoxy functional groups are attached; carboxylic acid, keto,

and 5- and 6-membered lactol groups decorate the edge.[9−12] Moreover, there exist nonoxidized sp^2 segments that are either aromatic or conjugated.[11] We hypothesize that in a similar fashion to CNTs, hydroxyl radicals will further oxidize GO via both the conversion of oxygen moieties to higher oxidation states and electrophilic addition to unsaturated bonds. The latter process will result in the formation of hydroxyl groups, which, in turn, can be further oxidized by the former mechanism.

As evidenced from the NMR and MS data, aromatic protons are formed from GO via a decarboxylation mechanism. Therefore, DFT calculations were implemented to acquire greater insight into decarboxylation. To this end, initially GQDs were functionalized with both a carboxylic acid and a keto group, which could be present on either an armchair edge (Figure 6A) or a zigzag edge (Figure 6B). The probable transition state consists of the conversion of the keto to an alcohol through the deprotonation of the acid followed by the decarboxylation of the carboxylic acid to CO$_2$ (g). In this case, the transition state is ∼0.6 eV higher than the initial state for the armchair edge (Figure 6A) and ∼2.3 eV higher for the zigzag configuration (Figure 6B). It should be noted that in solution these transitions states would be lower in energy than
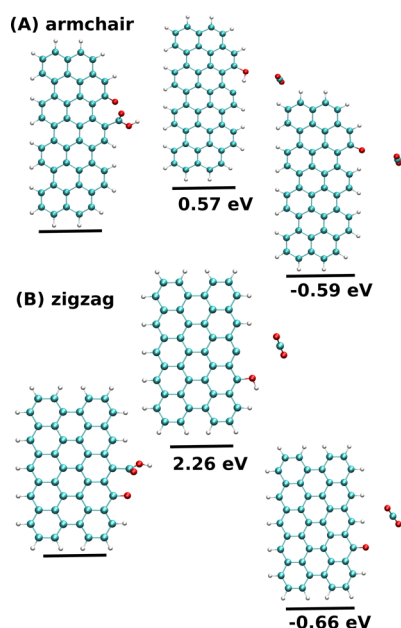
Figure 6. The initial configuration (left), the transition state, where the proton of the carboxylic acid jumps to the carbonyl group and the CO_2 desorbs in the gas phase (center), and the final configuration of the GQD, where the proton returns to the location to which the carboxylic acid existed to satisfy the dangling bond (right) for (A) armchair and (B) zigzag configurations of a GQD based on DFT calculations.

predicted by this simple model, as a proton can easily be transferred from solution to satisfy the dangling bond of the peripheral carbon atom in the GQD that was bonded to the carboxylic group. The relatively high-energy barrier of the transition state in the zigzag configuration indicates that the dangling bond is highly unsaturated compared to the armchair termination. The final state consists of the formation of a keto group, where the proton jumps back to the location where the carboxylic acid existed to satisfy the dangling bond; the final state is ~0.6 eV lower than the initial state for the armchair edge (Figure 6A) and ~0.7 eV lower for the zigzag edge (Figure 6B). Although the present model ignores solvent effects and defects, the results show that the decarboxylation is exothermic and thermodynamically very favorable.

AFM and fluorescence spectroscopy provided plausible evidence that GQDs were being formed via the photo-Fenton reaction, consistent with the literature.[20] Accordingly, the flakes of GO, which initially demonstrated a broad distribution of 589 ± 700 nm, underwent significant oxidation whereby the flake size was reduced to 36 ± 10 nm. To this end, GO is oxidized by hydroxyl radicals, which were generated via the photo-Fenton reaction, to yield nanometer-sized aromatic sp^2 domains that are surrounded by oxygen moieties along the edges.[21] These aromatic domains should be the source of the GQDs fluorescent properties.[21] This result was observed experimentally: the fluorescence intensity was ~19 times greater for the GQD products at day 3 versus GO at day 0 at an emission wavelength of 440 nm.

MS analyses support the degradation of photo-Fenton oxidized GO into GQDs through the formation of intermediate structures that are highly conjugated and full of carboxylic and hydroxyl moieties. In order to understand the fragmentation nature of carboxylic acid groups on aromatic structures, mellitic acid was investigated in the Orbitrap MS. A precursor mass spectrum reveals a protonated precursor and abundant ions

representing the loss of one, two, and three water molecules from the precursor (Supporting Information Figure S11). Anhydrous forms of mellitic acid are more stable than the protonated precursor under gas-phase MS conditions (Supporting Information Figure S11A). Following MS/MS, the fragmentation patterns show that the precursor is lost and multiple species representing losses of CO and CO_2 neutrals from the anhydride group are observed (Supporting Information Figure S11B). The sequential losses from the anhydride lead to the formation of stable gas-phase species.

The behavior of mellitic and phthlatic acid with positive mode ESI-MS can be used to make the following assumptions about the day 1 degradation parent MS spectra. (1) The degradation spectra contain signal from the protonated precursor and peaks associated with loss of neutrals (i.e., H_2O, CO, and CO_2) for carboxylic acids. (2) The degradation spectra may also contain a signal from the acid with different cations (i.e, H^+, Na^+, K^+, and Ca^{2+}) which is expected for ESI.[63] These two factors add to the complexity of the parent MS data for degradation products. Furthermore, the coisolation of precursors that are close in m/z produces MS/MS spectra that are difficult to assign at the resolving power of the Orbitrap.

It is apparent from the MS and MS/MS data, however, that phthalate species exist.[64,65] In addition to the low m/z peaks that correspond to phthalic anhydride and acid, several peaks with higher m/z show losses corresponding to neutral phthalic anhydride or acid molecules (low ppm Orbitrap errors). Such species may arise from homogeneous and heterogeneous clusters of phthalate species with various cations. The presence of a peak at m/z 149.024 is diagnostic for phthalates detected by various ionization sources in MS.[64−66] This ion is present in the ESI-Orbitrap MS data for degradation samples. Phthalates are common contaminants in plasticizers[67] and arise as background ions in ESI-MS.[68] The presence of these species in GO degradation samples indicates either their formation during degradation of GO flakes or increased extraction of these species from sample vials after the degradation process. Samples were handled in glassware during the degradation and transferred to Eppendorf vials for MS analysis. Thus, the introduction of these species could only arise after the degradation process from the pipet tips, Eppendorf vials, or solvents used for MS analysis if they were not present a priori in the sample. The magnitude of signals corresponding to the protonated phthalic anhydride (m/z 149.024) and phthalic acid (m/z 167.040) peaks increases by three and two orders of magnitude from day 0 (control) to day 1 samples. There is a decrease in the relative signal of these peaks of 92 and 43%, respectively, from day 1 to day 3 samples. Further separation prior to MS will be necessary in order to fully understand all of the observed degradation products.

In summary, the flakes of GO underwent morphological changes and resulted in the production of GQDs as evidenced by AFM; this transformation is indicative of oxidation/degradation driven via the photo-Fenton reaction. MS analysis demonstrated that intermediate products were formed during the conversion of GO into GQDs. By combining MS, NMR, and ATR-FTIR data, plausible structure(s) of these intermediate products, which largely consist of adjacent aromatic rings with carboxylic acid groups, are proposed. Furthermore, DFT calculations demonstrated that the decarboxylation step is both exothermic and thermodynamically very favorable. Given that carbon nanomaterials such as graphene and carbon nanotubes are likely to undergo transformations including

degradation that results in the formation of oxidized products[22−26] that may demonstrate toxicity,[27] our research represents an important step forward toward understanding the medical and environmental implications of such a promising nanomaterial.

■ ASSOCIATED CONTENT

Ⓢ Supporting Information

AFM images, length distributions, and section analysis of in solution GO samples with time; AFM images and section analysis of on the chip GO samples with time; AFM images of control experiments; Raman spectra; precursor scan spectra derived from ESI FT-ICR and ESI-Orbitrap MS for GO that reacted for 1 day under photo-Fenton conditions; ESI-Orbitrap MS and MS/MS data spectra of phthalic acid and GO after 1 day of the photo-Fenton reaction; NMR spectra; ATR-FTIR spectra; the precursor mass spectrum and fragmentation pattern of mellitic acid; accurate masses of the 20 most abundant species observed by FT-ICR MS. This material is available free of charge via the Internet at http://pubs.acs.org.

■ AUTHOR INFORMATION

Corresponding Author
*E-mail: astar@pitt.edu.
Notes
The authors declare no competing financial interest.

■ ACKNOWLEDGMENTS

■ REFERENCES

(1) Geim, A. K.; Novoselov, K. S. The Rise of Graphene. *Nat. Mater.* **2007**, *6*, 183−191.

(2) Zhu, Y.; Murali, S.; Cai, W.; Li, X.; Suk, J. W.; Potts, J. R.; Ruoff, R. S. Graphene and Graphene Oxide: Synthesis, Properties, and Applications. *Adv. Mater.* **2010**, *22*, 3906−3924.

(3) Lee, C.; Wei, X.; Kysar, J. W.; Hone, J. Measurement of the Elastic Properties and Intrinsic Strength of Monolayer Graphene. *Science* **2008**, *321*, 385−388.

(4) Geim, A. K. Graphene: Status and Prospects. *Science* **2009**, *324*, 1530−1534.

(5) Allen, M. J.; Tung, V. C.; Kaner, R. B. Honeycomb Carbon: A Review of Graphene. *Chem. Rev.* **2010**, *110*, 132−45.

(6) Kauffman, D. R.; Star, A. Graphene versus Carbon Nanotubes for Chemical Sensor and Fuel Cell Applications. *Analyst* **2010**, *135*, 2790−2797.

(7) Dreyer, D. R.; Park, S.; Bielawski, C. W.; Ruoff, R. S. The Chemistry of Graphene Oxide. *Chem. Soc. Rev.* **2010**, *39*, 228−240.

(8) Park, S.; Ruoff, R. S. Chemical Methods for the Production of Graphenes. *Nat. Nanotechnol.* **2009**, *4*, 217−224.

(9) He, H.; Riedl, T.; Lerf, A.; Klinowski, J. Solid-State NMR Studies of the Structure of Graphite Oxide. *J. Phys. Chem.* **1996**, *100*, 19954−19958.

(10) He, H.; Klinowski, J.; Forster, M.; Lerf, A. A New Structural Model for Graphite Oxide. *Chem. Phys. Lett.* **1998**, *287*, 53−56.

(11) Lerf, A.; He, H.; Forster, M.; Klinowski, J. Structure of Graphite Oxide Revisited. *J. Phys. Chem. B* **1998**, *102*, 4477−4482.

(12) Cai, W.; Piner, R. D.; Stadermann, F. J.; Park, S.; Shaibat, M. A.; Ishii, Y.; Yang, D.; Velamakanni, A.; An, S. J.; Stoller, M.; et al. Synthesis and Solid-State NMR Structural Characterization of ¹³C-Labeled Graphite Oxide. *Science* **2008**, *321*, 1815−1817.

(13) Shen, J.-H.; Zhu, Y.-H.; Chen, C.; Yang, X.-L.; Li, C.-Z. Facile Preparation and Upconversion Luminescence of Graphene Quantum Dots. *Chem. Commun.* **2011**, *47*, 2580−2582.

(14) Shen, J.; Zhu, Y.; Yang, X.; Zong, J.; Zhang, J.; Li, C. One-Pot Hydrothermal Synthesis of Graphene Quantum Dots Surface-Passivated by Polyethylene Glycol and Their Photoelectric Conversion under Near-Infrared Light. *New J. Chem.* **2012**, *36*, 97−101.

(15) Pan, D.; Zhang, J.; Li, Z.; Wu, M. Hydrothermal Route for Cutting Graphene Sheets into Blue-Luminescent Graphene Quantum Dots. *Adv. Mater.* **2010**, *22*, 734−738.

(16) Pan, D.; Guo, L.; Zhang, J.; Xi, C.; Xue, Q.; Huang, H.; Li, J.; Zhang, Z.; Yu, W.; Chen, Z.; et al. Cutting sp² Clusters in Graphene Sheets into Colloidal Graphene Quantum Dots with Strong Green Fluorescence. *J. Mater. Chem.* **2012**, *22*, 3314−3318.

(17) Zhu, S.; Zhang, J.; Qiao, C.; Tang, S.; Li, Y.; Yuan, W.; Li, B.; Tian, L.; Liu, F.; Hu, R.; et al. Strongly Green-Photoluminescent Graphene Quantum Dots for Bioimaging Applications. *Chem. Commun.* **2011**, *47*, 6858−6860.

(18) Zhu, S.; Zhang, J.; Liu, X.; Li, B.; Wang, X.; Tang, S.; Meng, Q.; Li, Y.; Shi, C.; Hu, R.; et al. Graphene Quantum Dots with Controllable Surface Oxidation, Tunable Fluorescence and Up-Conversion Emission. *RSC Adv.* **2012**, *2*, 2717−2720.

(19) Li, L.-L.; Ji, J.; Fei, R.; Wang, C.-Z.; Lu, Q.; Zhang, J.-R.; Jiang, L.-P.; Zhu, J.-J. A Facile Microwave Avenue to Electrochemilumines-cent Two-Color Graphene Quantum Dots. *Adv. Funct. Mater.* **2012**, *22* (2971−2979), S2971/1−S2971/5.

(20) Zhou, X.; Zhang, Y.; Wang, C.; Wu, X.; Yang, Y.; Zheng, B.; Wu, H.; Guo, S.; Zhang, J. Photo-Fenton Reaction of Graphene Oxide: A New Strategy to Prepare Graphene Quantum Dots for DNA Cleavage. *ACS Nano* **2012**, *6*, 6592−6599.

(21) Li, L.; Wu, G.; Yang, G.; Peng, J.; Zhao, J.; Zhu, J.-J. Focusing on Luminescent Graphene Quantum Dots: Current Status and Future Perspectives. *Nanoscale* **2013**, *5*, 4015−4039.

(22) Allen, B. L.; Kichambare, P. D.; Gou, P.; Vlasova, I. I.; Kapralov, A. A.; Konduru, N.; Kagan, V. E.; Star, A. Biodegradation of Single-Walled Carbon Nanotubes through Enzymatic Catalysis. *Nano Lett.* **2008**, *8*, 3899−3903.

(23) Kagan, V. E.; Konduru, N. V.; Feng, W.; Allen, B. L.; Conroy, J.; Volkov, Y.; Vlasova, I. I.; Belikova, N. A.; Yanamala, N.; Kapralov, A.; et al. Carbon Nanotubes Degraded by Neutrophil Myeloperoxidase Induce Less Pulmonary Inflammation. *Nat. Nanotechnol.* **2010**, *5*, 354−359.

(24) Russier, J.; Menard-Moyon, C.; Venturelli, E.; Gravel, E.; Marcolongo, G.; Meneghetti, M.; Doris, E.; Bianco, A. Oxidative Biodegradation of Single- and Multi-Walled Carbon Nanotubes. *Nanoscale* **2011**, *3*, 893−896.

(25) Kotchey, G. P.; Hasan, S. A.; Kapralov, A. A.; Ha, S. H.; Kim, K.; Shvedova, A. A.; Kagan, V. E.; Star, A. A Natural Vanishing Act: The Enzyme-Catalyzed Degradation of Carbon Nanomaterials. *Acc. Chem. Res.* **2012**, *45*, 1770−1781.

(26) Kotchey, G. P.; Zhao, Y.; Kagan, V. E.; Star, A. Peroxidase-mediated Biodegradation of Carbon Nanotubes *in vitro* and *in vivo*. *Adv. Drug Delivery Rev.* **2013**, *65*, 1921−1932.

(27) Pan, S.; Sardesai, N. P.; Liu, H.; Li, D.; Rusling, J. F. Assessing DNA Damage from Enzyme-Oxidized Single-Walled Carbon Nano-tubes. *Toxicol. Res.* **2013**, *2*, 375−378.

(28) Fenton, H. J. H. LXXIII.-Oxidation of Tartaric Acid in Presence of Iron. *J. Chem. Soc.* **1894**, *65*, 899−910.

(29) Walling, C. Fentons Reagent Revisited. *Acc. Chem. Res.* **1975**, *8*, 125−131.

(30) Bauer, R.; Fallmann, H. The Photo-Fenton Oxidation - A Cheap and Efficient Wastewater Treatment Method. *Res. Chem. Intermed.* **1997**, *23*, 341−354.

(31) Ikehata, K.; El-Din, M. G. Aqueous Pesticide Degradation by Hydrogen Peroxide/Ultraviolet Irradiation and Fenton-type Advanced Oxidation Processes: A Review. *J. Environ. Eng. Sci.* **2006**, *5*, 81−135.

(32) Lee, S.; Oh, J.; Park, Y. Degradation of Phenol with Fenton-like Treatment by Using Heterogeneous Catalyst (Modified Iron Oxide) and Hydrogen Peroxide. *Bull. Korean Chem. Soc.* **2006**, *27*, 489−494.

(33) Palmroth, M. R.; Langwaldt, J. H.; Aunola, T. A.; Goi, A.; Puhakka, J. A.; Tuhkanen, T. A. Treatment of PAH-contaminated Soil by Combination of Fenton's Reaction and Biodegradation. *J. Chem. Technol. Biotechnol.* **2006**, *81*, 598−607.

(34) Barreiro, J. C.; Capelato, M. D.; Martin-Neto, L.; Bruun Hansen, H. C. Oxidative Decomposition of Atrazine by a Fenton-like Reaction in a H_2O_2/Ferrihydrite System. *Water Res.* **2007**, *41*, 55−62.

(35) Jonsson, S.; Persson, Y.; Frankki, S.; van Bavel, B.; Lundstedt, S.; Haglund, P.; Tysklind, M. Degradation of Polycyclic Aromatic Hydrocarbons (PAHs) in Contaminated Soils by Fenton's Reagent: A Multivariate Evaluation of the Importance of Soil Characteristics and PAH Properties. *J. Hazard. Mater.* **2007**, *149*, 86−96.

(36) Liao, Q.; Sun, J.; Gao, L. Degradation of Phenol by Heterogeneous Fenton Reaction using Multi-Walled Carbon Nanotube Supported Fe_2O_3 Catalysts. *Colloid. Surface A* **2009**, *345*, 95−100.

(37) Lloyd, R. V.; Hanna, P. M.; Mason, R. P. The Origin of the Hydroxyl Radical Oxygen in the Fenton Reaction. *Free Radical Biol. Med.* **1997**, *22*, 885−888.

(38) Zhao, B. X.; Li, X. Z.; Wang, P. 2,4-Dichlorophenol Degradation by an Integrated Process: Photoelectrocatalytic Oxidation and E-Fenton Oxidation. *Photochem. Photobiol.* **2007**, *83*, 642−646.

(39) Fan, C. L.; Li, W.; Li, X.; Zhao, S. J.; Zhang, L.; Mo, Y. J.; Cheng, R. M. Efficient Photo-Assisted Fenton Oxidation Treatment of Multi-Waited Carbon Nanotubes. *Chin. Sci. Bull.* **2007**, *52*, 2054−2062.

(40) Kaiser, N.; Quinn, J.; Blakney, G.; Hendrickson, C.; Marshall, A. A Novel 9.4 T FTICR Mass Spectrometer with Improved Sensitivity, Mass Resolution, and Mass Range. *J. Am. Soc. Mass Spectrom.* **2011**, *22*, 1343−1351.

(41) Kaiser, N. K.; Savory, J. J.; McKenna, A. M.; Quinn, J. P.; Hendrickson, C. L.; Marshall, A. G. Electrically Compensated Fourier Transform Ion Cyclotron Resonance Cell for Complex Mixture Mass Analysis. *Anal. Chem.* **2011**, *83*, 6907−6910.

(42) Emmett, M. R.; White, F. M.; Hendrickson, C. L.; Shi, S. D. H.; Marshall, A. G. Application of Micro-Electrospray Liquid Chromatography Techniques to FT-ICR MS to Enable High-Sensitivity Biological Analysis. *J. Am. Soc. Mass Spectrom.* **1998**, *9*, 333−340.

(43) Emmett, M. R.; Caprioli, R. M. Micro-Electrospray Mass Spectrometry: Ultra-High-Sensitivity Analysis of Peptides and Proteins. *J. Am. Soc. Mass Spectrom.* **1994**, *5*, 605−613.

(44) Marshall, A. G.; Wang, T. C. L.; Ricca, T. L. Tailored Excitation for Fourier Transform Ion Cyclotron Mass Spectrometry. *J. Am. Chem. Soc.* **1985**, *107*, 7893−7897.

(45) Guan, S.; Marshall, A. G. Stored Waveform Inverse Fourier transform (SWIFT) Ion Excitation in Trapped-Ion Mass Spectometry: Theory And Applications. *Int. J. Mass Spectrom. Ion Processes* **1996**, *157−158*, 5−37.

(46) Håkansson, K.; Chalmers, M. J.; Quinn, J. P.; McFarland, M. A.; Hendrickson, C. L.; Marshall, A. G. Combined Electron Capture and Infrared Multiphoton Dissociation for Multistage MS/MS in a Fourier Transform Ion Cyclotron Resonance Mass Spectrometer. *Anal. Chem.* **2003**, *75*, 3256−3262.

(47) Bythell, B.; Hendrickson, C.; Marshall, A. Relative Stability of Peptide Sequence Ions Generated by Tandem Mass Spectrometry. *J. Am. Soc. Mass Spectrom.* **2012**, *23*, 644−654.

(48) Blakney, G. T.; Hendrickson, C. L.; Marshall, A. G. Predator Data Station: A Fast Data Acquisition System for Advanced FT-ICR MS Experiments. *Int. J. Mass Spectrom.* **2011**, *306*, 246−252.

(49) Marshall, A. G.; Verdun, F. R. *Fourier Transforms in Optical, NMR, and Mass Spectrometry: A User's Handbook*; Elsevier: Amsterdam, 1990.

(50) Ledford, E. B.; Rempel, D. L.; Gross, M. L. Space Charge Effects in Fourier Transform Mass Spectrometry. II. Mass Calibration. *Anal. Chem.* **1984**, *56*, 2744−2748.

(51) Frisch, M. J.; Trucks, G. W.; Schlegel, H. B.; Scuseria, G. E.; Robb, M. A.; Cheeseman, J. R.; Scalmani, G.; Barone, V.; Mennucci, B.; Petersson, G. A.; Nakatsuji, H.; Caricato, M.; Li, X.; Hratchian, H. P.; Izmaylov, A. F.; Bloino, J.; Zheng, G.; Sonnenberg, J. L.; Hada, M.; Ehara, M.; Toyota, K.; Fukuda, R.; Hasegawa, J.; Ishida, M.; Nakajima, T.; Honda, Y.; Kitao, O.; Nakai, H.; Vreven, T.; Montgomery, J. A., Jr.; Peralta, P. E.; Ogliaro, F.; Bearpark, M.; Heyd, J. J.; Brothers, E.; Kudin, K. N.; Staroverov, V. N.; Kobayashi, R.; Normand, J.; Raghavachari, K.; Rendell, A.; Burant, J. C.; Iyengar, S. S.; Tomasi, J.; Cossi, M.; Rega, N.; Millam, N. J.; Klene, M.; Knox, J. E.; Cross, J. B.; Bakken, V.; Adamo, C.; Jaramillo, J.; Gomperts, R.; Stratmann, R. E.; Yazyev, O.; Austin, A. J.; Cammi, R.; Pomelli, C.; Ochterski, J. W.; Martin, R. L.; Morokuma, K.; Zakrzewski, V. G.; Voth, G. A.; Salvador, P.; Dannenberg, J. J.; Dapprich, S.; Daniels, A. D.; Farkas, Ö.; Ortiz, J. V.; Cioslowski, J.; Fox, D. J. *Gaussian 09*, revision D.01 ; Gaussian, Inc.: Wallingford, CT, 2009

(52) Becke, A. D. Density-Functional Thermochemistry. III. The Role of Exact Exchange. *J. Chem. Phys.* **1993**, *98*, 5648−5652.

(53) Lee, C.; Yang, W.; Parr, R. G. Development of the Colle-Salvetti Correlation-Energy Formula into a Functional of the Electron Density. *Phys. Rev. B* **1988**, *37*, 785−789.

(54) Vosko, S. H.; Wilk, L.; Nusair, M. Accurate Spin-Dependent Electron Liquid Correlation Energies for Local Spin Density Calculations: A Critical Analysis. *Can. J. Phys.* **1980**, *58*, 1200−1211.

(55) Stephens, P. J.; Devlin, F. J.; Chabalowski, C. F.; Frisch, M. J. Ab Initio Calculation of Vibrational Absorption and Circular Dichroism Spectra Using Density Functional Force Fields. *J. Phys. Chem.* **1994**, *98*, 11623−11627.

(56) McLean, A. D.; Chandler, G. S. Contracted Gaussian Basis Sets for Molecular Calculations. I. Second Row Atoms, Z=11−18. *J. Chem. Phys.* **1980**, *72*, 5639−5648.

(57) Krishnan, R.; Binkley, J. S.; Seeger, R.; Pople, J. A. Self-Consistent Molecular Orbital Methods. XX. A Basis Set for Correlated Wave Functions. *J. Chem. Phys.* **1980**, *72*, 650−654.

(58) Stankovich, S.; Piner, R. D.; Chen, X.; Wu, N.; Nguyen, S. T.; Ruoff, R. S. Stable Aqueous Dispersions of Graphitic Nanoplatelets via the Reduction of Exfoliated Graphite Oxide in the Presence of Poly(sodium 4-styrenesulfonate). *J. Mater. Chem.* **2006**, *16*, 155−158.

(59) Stankovich, S.; Dikin, D. A.; Dommett, G. H. B.; Kohlhaas, K. M.; Zimney, E. J.; Stach, E. A.; Piner, R. D.; Nguyen, S. T.; Ruoff, R. S. Graphene-Based Composite Materials. *Nature* **2006**, *442*, 282−286.

(60) Dresselhaus, M. S.; Jorio, A.; Hofmann, M.; Dresselhaus, G.; Saito, R. Perspectives on Carbon Nanotubes and Graphene Raman Spectroscopy. *Nano Lett.* **2010**, *10*, 751−758.

(61) Acik, M.; Lee, G.; Mattevi, C.; Chhowalla, M.; Cho, K.; Chabal, Y. J. Unusual Infrared-Absorption Mechanism in Thermally Reduced Graphene Oxide. *Nat. Mater.* **2010**, *9*, 840−845.

(62) Li, W.; Bai, Y.; Zhang, Y.; Sun, M.; Cheng, R.; Xu, X.; Chen, Y.; Mo, Y. Effect of Hydroxyl Radical on the Structure of Multi-Walled Carbon Nanotubes. *Synth. Met.* **2005**, *155*, 509−515.

(63) Habicht, S. C.; Vinueza, N. R.; Archibold, E. F.; Duan, P.; Kenttamaa, H. I. Identification of the Carboxylic Acid Functionality by Using Electrospray Ionization and Ion−Molecule Reactions in a Modified Linear Quadrupole Ion Trap Mass Spectrometer. *Anal. Chem.* **2008**, *80*, 3416−3421.

(64) Jeilani, Y. A.; Cardelino, B. H.; Ibeanusi, V. M. Positive chemical Ionization Triple-Quadrupole Mass Spectrometry and Ab Initio Computational Studies of the Multi-Pathway Fragmentation of Phthalates. *J. Mass Spectrom.* **2010**, *45*, 678−685.

(65) Earls, A. O.; Axford, I. P.; Braybrook, J. H. Gas Chromatography−Mass Spectrometry Determination of the Migration of Phthalate Plasticisers from Polyvinyl Chloride Toys and Childcare Articles. *J. Chromatogr. A* **2003**, *983*, 237−246.

(66) Silva, P. J.; Prather, K. A. Interpretation of Mass Spectra from Organic Compounds in Aerosol Time-of-Flight Mass Spectrometry. *Anal. Chem.* **2000**, *72*, 3553−3562.

(67) Kamrin, M. A. Phthalate Risks, Phthalate Regulation, and Public Health: A Review. *J. Toxicol. Environ. Health, Part B* **2009**, *12*, 157−174.

(68) Weber, R. J. M.; Li, E.; Bruty, J.; He, S.; Viant, M. R. MaConDa: A Publicly Accessible Mass Spectrometry Contaminants Database. *Bioinformatics* **2012**, *28*, 2856−2857.